388 Vol. 40, No. 2 / February 2023 / Journal of the Optical Society of America B Research Article

Journal of the Optical Society of America B

OPTICAL PHYSICS

# Multifunctional and tunable ultra-broadband linear to circle polarization converter based on $VO_2$-integrated material

Zhen Qiao,[1,2] Rujia Cao,[1] Siyuan Liao,[1] and Haifeng Zhang[1,*]

[1]College of Electronic and Optical Engineering & College of Flexible Electronics (Future Technology), Nanjing University of Posts and Telecommunications, Nanjing 210023, China
[2]e-mail: 1159258114@qq.com
*Corresponding author: hanlor@163.com

Received 16 November 2022; revised 24 December 2022; accepted 1 January 2023; posted 5 January 2023; published 30 January 2023

**Considering that the metastructures (MSs) previously proposed usually perform in a single state, herein, a multifunctional and tunable ultra-broadband linear to circle (LTC) polarization converter based on phase transition material vanadium dioxide ($VO_2$) is proposed in the terahertz (THz) region. By manipulating the temperature, the function of the LTC polarization conversion (PC) can be conveniently switched between transmission and reflection states. When the environment temperature is low, $VO_2$ presents the insulating state, and the MS can achieve ultra-wideband LTC PC from 0.57–0.83 THz with a relative bandwidth (RB) of 37.3%. When the temperature exceeds 68°C, LTC PC with the frequency bandwidth of 0.83–1.20 THz and 0.83–1.17 THz can be obtained in a reflection state when electromagnetic waves propagate forward and backward, whose RBs are 36.4% and 34.0%, respectively. Meanwhile, a broadband linear to linear (LTL) PC can also be realized in the range of 1.19–1.41 THz for the forward incident wave and 1.16–1.37 THz for the backward incident wave. The designed MS offers an effective method to realize four different functions and has tremendous potential value in realizing THz modulation devices, electromagnetic cloaking, and communication systems.** 

https://doi.org/10.1364/JOSAB.481286

## 1. INTRODUCTION

Benefiting from the sub-wavelength periodic structure [1], electromagnetic (EM) metamaterial can be designed as synthetic composite structures with arbitrary permittivity [2] and magnetic permeability [3], thus possessing numerous exotic properties and functions that are not found in nature. A metastructure (MS) is a three-dimensional metamaterial, which has developed from a metasurface. Hence, the MS plays an essentially standing role in antennas [4], absorbers [5], polarization conversion (PC) [6], and remote sensing [7], which has become a novel research hotspot. With the rapid proliferation of technology and science, the application of EM waves is becoming increasingly common. Thus, controlling and manipulating the polarization states of EM waves is particularly critical. Many polarization converters have been proposed to obtain superior performances in EM applications [8–10]. Due to the cumbersome volume [11] and the demanding requirements for materials, the conventional EM polarization converter, which is achieved with twisted nematic liquid crystal [12] and dichroic solid crystal [13], cannot meet the basic needs of our daily life. Fortunately, consisting of periodic sub-wavelength units, the MS provides a better platform for us to overcome the tough situation confronted by the limit of bulky volume and unlock the key bottleneck of manipulation of EM characteristics.

In the advancement of terahertz (THz) functional devices, it has been confirmed that THz waves have two different polarization states [14,15]. In addition to linear polarized (LP) waves with more availability and universality, the research on circularly polarized (CP) waves is extensive and in-depth as well due to the robustness and chirality. Polarization converters, which can control the characteristics of EM waves such as phase, amplitude, and state, are widely applied in responding to increasingly complex EM circumstances and communication demands [16,17]. Up to this day, it has not been an uncommon occurrence to explore various design schemes of PC already [18,19]. For instance, a linear polarization converter was proposed by Grady *et al*. [20] in 2013, which was made of short metal wires in the reflection state, realizing the change of polarization state in the range of 0.8–1.8 THz. Zhang *et al*. [10] presented a reflective polarization converter that contains disk resonators and split-ring resonators with a 76.19% relative bandwidth (RB) in 2016. Based on crescent-shaped MSs, Nguyen *et al*. [21] proposed a wideband reflective linear polarization converter, and experiments have proved that the polarization conversion rate (PCR) is more than 90% for a wide bandwidth of 6 GHz covering the

entire Ku-band. Apart from linear to linear (LTL) polarization, the manipulation of CP waves is also quite meaningful and significant. By virtue of numerous irreplaceable advantages, such as low sensitivity to multiple paths and atmospheric effects of reflection and absorption, CP waves have become more popular in civilian and military applications. In 2021, Wang *et al*. [22] successfully introduced a structure with two metal strips and an I-shaped strip to obtain reflected CP waves in the ranges of 15–21.2 GHz and 27–30.3 GHz. A dual-rotational-direction linear to circle (LTC) polarization converter was designed by Liu *et al*. [23] in 2022, which operates in dual-band in 29.0–41.5 GHz and 52.5–61.5 GHz. In summary, though having a relatively wide bandwidth, these polarization converters only operate in a single function or state.

Nevertheless, due to the complex working environment and the trend of integration, converters with only a single function or fixed operating band appear fatigued to meet the vigorous technological evolution. By virtue of the research into tunable materials, there are various methods to make the device multifunctional, including but not limited to electric fields [24], temperature [25], and illumination [26]. Vanadium dioxide ($VO_2$) is recognized to exhibit its thermally driven phase transition from insulator to metal when the critical temperature approaches nearly 68°C [27–29]. In general, $VO_2$ presents the insulating or the semiconducting state when the temperature is below 68°C. In this condition, it is considered that the conductivity of $VO_2$ with the monoclinic lattice structure is 0 S m$^{-1}$ [30]. Conversely, when the temperature exceeds 68°C [31], the structure of $VO_2$ is rearranged into a tetragonal lattice [32]. Then, $VO_2$ behaves as a metallic state, and the conductivity can be approximated as $3 \times 10^5$ S m$^{-1}$ [33,34]. $VO_2$ stands out for its rapid and sudden phase transition, which has a low phase transition temperature and can be easily achieved by thermostats. The tunable conductivity of $VO_2$ causes it to have a wide range of potential applications in electronic [27] and optical [33] devices. To elucidate, Yahiaoui *et al*. [35] presented a LTL single-layer THz metasurface, whose operating band can be broadened as the $VO_2$ transforms from the insulator to the metallic phase. Moreover, a reflective dual-functional THz device based on $VO_2$ is presented by Yan *et al*. [36], which can convert from LTL PC to LTC PC as the temperature rises.

By virtue of the phase transition material of $VO_2$, the converters mentioned above surmount the untenable defect of conventional polarization converters [37]. Nonetheless, they are merely operating in a single reflection or transmission state. Since there are few studies on the converter whose function can combine transmission and reflection simultaneously, herein, a multifunctional and tunable ultra-broadband polarization converter is proposed in this paper. By manipulating the phase transition of $VO_2$, the proposed MS possesses four different functions, and CP waves can be obtained both in the transmission and reflection states while the linear waves are incident. $VO_2$ is inserted into the middle layer so that the function states can be switched between transmission and reflection states conveniently at different temperatures. With a RB of 37.1%, the proposed MS achieves the axial ratio (AR) <3 dB operating bandwidth region from 0.57 THz to 0.83 THz in the transmission state when $VO_2$ is at a low temperature. As the temperature exceeds 68°C, the $VO_2$ presents a metallic state, which means that the MS function is in a reflection state. For the forward and backward propagation incident EM waves, LTC PC in the frequency band range of 0.83–1.20 THz and 0.83–1.17 THz can be realized with RBs of 36.4% and 34.0%, respectively. Meanwhile, the LTL PC can also be achieved in the broadband of 1.19–1.41 THz with a RB of 16.9% for the forward incident waves and 1.16–1.37 THz with a RB of 16.6% for the backward incident waves. Such a MS possesses the merits of multifunctional collaborative processing and wide operating frequencies, enriching the design of multifunctional devices and providing potential applications in the THz region [24,33,36].

## 2. STRUCTURE

The schematic view of the proposed MS is manifested in Fig. 1, demonstrating certain information regarding the incident waves. In general, the MS consists of three dielectric substrates with different thicknesses. The lossy polyimide with permittivity of 3.5 and loss tangent of 0.0027 [38] has been chosen as the dielectric material. Besides, a multi-metal layer structure is adopted by the MS, and gold with a conductivity of $4.561 \times 10^7$ s/m [39] is used as the material of the metal resonators, which are depicted in yellow. The period is designed as $p = 80$ μm, and the metallic plates are 0.2 μm thick as revealed in Fig. 2(d).

To grasp the composition of MS more evidently, in Fig. 2, the detailed schematic views of the mentioned MS unit from different perspectives as well as some parameter values are demonstrated. In Fig. 2(a), the arrangement relationship between the layers can be derived from the disassembled view of the MS. And the top metal resonator is X-shaped, as manifested in Fig. 2(b). Then, the second metal resonator is two pairs of C-shaped resonators with different sizes, which are placed on the dielectric substrate in Fig. 2(c). The opening sizes of the split resonators are $c_1 = 10$ μm and $c_2 = 8$ μm. Apart from the resonators in Fig. 2(c), the L-shaped backing plates, which highlight with bright blue, serve as connections and supports of the adjacent substrates. Accordingly, an air layer approximately forms between the two dielectric substrates. In this way, the phase or amplitude of the incident EM waves can be effectively adjusted. In Fig. 2(e), the middle gold layer is composed of a hollow metal piece together with the tunable material $VO_2$, which ensures that the proposed design can be switched between the transmission state and reflection state by manipulating

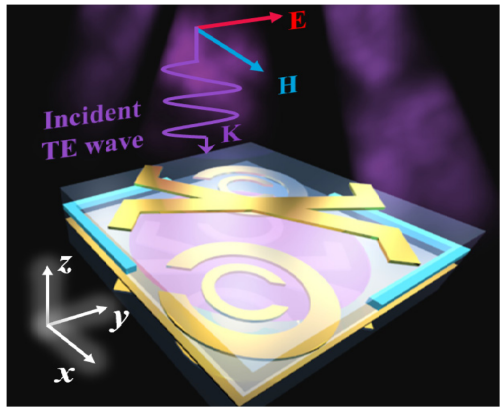


**Fig. 1.** Schematic view of the MS for the incident TE wave.

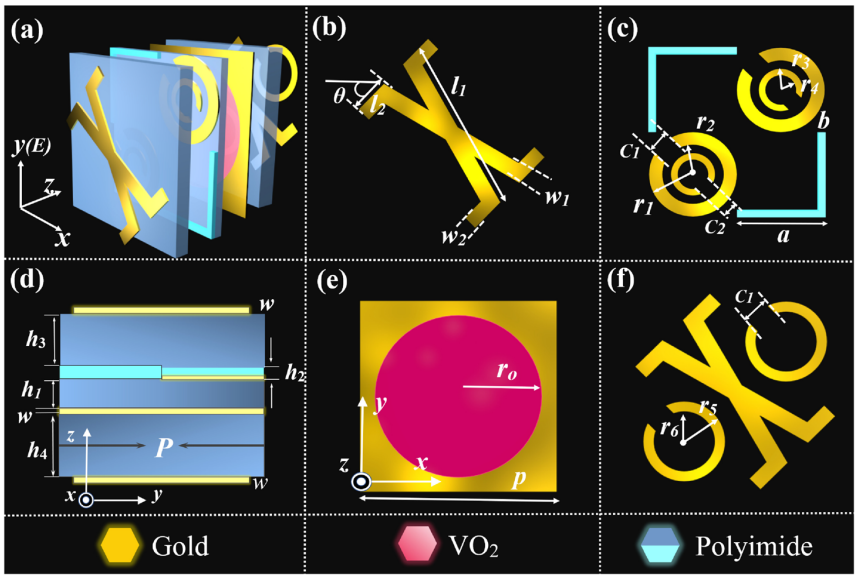


**Fig. 2.** Schematic views of the mentioned MS as observed from different perspectives: (a) decomposition view of the unit; (d) side view of the unit. (b), (c), (e), and (f) are the decomposition views of the unit.

**Table 1. Detailed Parameters and Values of the Proposed MS**

| Parameters | $p$ | $w$ | $r_0$ | $r_1$ | $r_2$ |
|---|---|---|---|---|---|
| Value (μm) | 80 | 0.2 | 34 | 20 | 14 |
| **Parameters** | $h_1$ | $h_2$ | $h_3$ | $h_4$ | $r_3$ |
| Value (μm) | 6 | 1.2 | 13 | 18 | 10 |
| **Parameters** | $r_4$ | $r_5$ | $r_6$ | $\theta$ | $l_1$ |
| Value (μm) | 7 | 12 | 16 | 45° | 70 |
| **Parameters** | $w_1$ | $l_2$ | $w_2$ | $a$ | $b$ |
| Value (μm) | 7 | 15 | 6 | 40 | 3 |

the temperature. And the bottom resonators also choose an X-shaped structure as the main resonant part and additionally contain a pair of C-shaped split resonator rings as demonstrated in Fig. 2(f). All the resonators are placed in a 45° direction off the $y$ axis, and further details on the structural parameters are presented in Table 1.

## 3. RESULT AND THEORETICAL ANALYSIS

To realize the control of the polarization state of THz waves, it is necessary to deduce the PC principle of LTC polarized waves. Regarded as a linear combination of the TE and TM waves, in other words, a CP wave can be decomposed into two orthogonal LP waves. Assuming that a LP wave is vertically incident at a polarization angle of 45°, the incident EM wave can be split into TE and TM waves equally. Herein, the transmission state is selected as an example. After the PC of the MS, the transmitted wave can be expressed as follows [10,40]:

$$E_t = E_{xt}\vec{e}_x + E_{yt}\vec{e}_y = t_{xx}e^{j\varphi_{xx}}E_{xinc}\vec{e}_x + t_{yy}e^{j\varphi_{yy}}E_{yinc}\vec{e}_y, \quad (1)$$

$$t_{ij} = \left|\frac{E_{it}}{E_{jinc}}\right|, \quad (2)$$

wherein $t$ refers to the transmission state, the subscript $j$ means the polarized states of the incident waves, and the subscript $i$ refers to the polarized states of the transmitted waves. So, $t_{xx}$ and $t_{yy}$ represent the unpolarized conversion part of the TE and TM waves, respectively. Additionally, $\varphi_{xx}$ and $\varphi_{yy}$ are expressed as the phase of the TE and TM waves.

To calculate the polarization state of the transmitted wave, the corresponding formulas are used as follows [40]:

$$S_1 = |t_{xx}|^2 + |t_{yy}|^2, \quad (3)$$

$$S_2 = |t_{xx}|^2 - |t_{yy}|^2, \quad (4)$$

$$S_3 = 2\,|t_{xx}|\,|t_{yy}|\cos(\Delta\varphi), \quad (5)$$

$$S_4 = 2\,|t_{xx}|\,|t_{yy}|\sin(\Delta\varphi). \quad (6)$$

If Eqs. (7) and (8) are simultaneously satisfied (where $n$ is the integer) [10,40], the condition of $S_4/S_1 = 1$ will be achieved. Eventually, the LTC PC can be realized,

$$t_{xx} = t_{yy}, \quad (7)$$

$$\Delta\varphi = \varphi_{yy} - \varphi_{xx} = 2n\pi + 0.5\pi. \quad (8)$$

Generally, there are two indices usually adopted to judge the quality of LTL PC and LTC PC, which are called the PCR and AR separately, as shown in Eqs. (9) and (10) [10,38,40]:

$$\mathrm{PCR} = \frac{t_{xy}^2}{t_{yy}^2 + t_{xy}^2 + r_{yy}^2 + r_{xy}^2}, \quad (9)$$

$$\mathrm{AR} = 10\lg\left(\tan\left(\frac{1}{2}\arcsin\left(\frac{S_4}{S_1}\right)\right)\right). \quad (10)$$

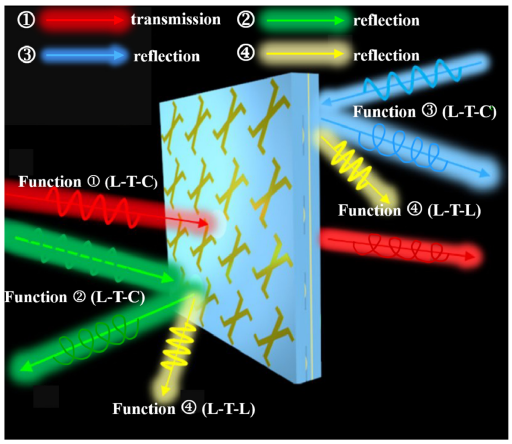


**Fig. 3.** Illustration of the four operating functions of the MS.

Normally, the operating band with AR < 3 dB is called the portion with a good circle characteristic, and the frequency band with a PCR greater than 90% is generally hoped to meet the LTL PC standard.

To better demonstrate the four functions of the proposed MS, Fig. 3 exhibits the wave propagation and PC information in different colors. By adjusting the environment temperature, $VO_2$ transforms from an insulating state to a metallic state, thus realizing a MS switch from the transmission to reflection.

Function ① is to achieve LTC PC in the transmission state under the low ambient temperature condition. Moreover, functions ②–④ are obtained when the $VO_2$ of the MS is thermally excited, operating in the reflection state. Functions ② and ③ are both anticipated to realize LTC PC. However, it is worth mentioning that the propagation directions of the incident waves under the two functions are quite different on the ground that ② is forward and the other is backward. So, it is feasible to take more comprehensive advantage of the MS when the incident waves are in different directions. In comparison to ①–③, function ④ has a completely different implementation in that it can generate the LTL PC from the $y$ axis to the $x$ axis with a broad working bandwidth for the waves of different incident directions. More intuitive information can be found in Table 2 below, and other details will be discussed in the later sections.

### A. Function ① for the Forward Propagating in the Transmission State

To start with, when the MS is at a low environment temperature, $VO_2$ is insulating. In this condition, the conductivity of the $VO_2$ is taken as 0 S $m^{-1}$. Therefore, the $VO_2$ in the middle layer can be considered as a transparent substrate, which can function to transmit.

In Fig. 4(a), the magnitudes of co-polarized and cross-polarized transmission coefficients ($t_{yy}$ and $t_{xy}$) are exhibited. The red curve denotes the amplitude of $t_{yy}$ while the amplitude of $t_{xy}$ is depicted by the blue line. The transmission coefficients are approximately equal from 0.57 THz to 0.83 THz, with a RB of 37.3%. The two curves fit very well especially from 0.63 THz to 0.73 THz, which extremely satisfies the equal amplitude condition in Eq. (7). Meanwhile, as exhibited in Fig. 4(b), the changing trend with the curves of $\varphi_{xy}$ and $\varphi_{yy}$ is consistent, and the phase difference $\Delta\varphi = \varphi_{xy} - \varphi_{yy}$ is about $2n\pi - \pi/2$, which means that Eq. (9) can also be satisfied simultaneously. As a result, the value of AR can be obtained in Fig. 4(c) by combining the amplitude and phase conditions. The AR drops to 3 dB at 0.57 THz and continues to decrease, reaching the resonance point at 0.71 THz. The value of AR is nearly dipped to zero, which means that a perfect CP wave can be generated at the resonance point. The operating bandwidth where AR is less than 3 dB is 0.57–0.83 THz with a RB of 37.3%, utilizing Eq. (10 ) for calculation, which reaches the ultra-wideband target.

To further expound the indispensability of the multi-metal layer structure and L-shaped backing plates, the phase diagram of the structure in which the X-shaped resonator and two pairs of C-shaped resonators are in the same top layer is also given in Fig. 4(d). Compared with Fig. 4(b), the overall phase shifts slightly to a higher frequency. Moreover, the phase matching deteriorates sharply on the edge of the high-frequency band highlighted by the black circle. Therefore, a multi-metal layer structure is required to increase the design freedom. Benefiting from these measures, the phase condition can be improved, and the operating band can be effectively broadened in this way.

To illustrate the working mechanism more clearly, the instantaneous electric fields at 0.71 THz are demonstrated in Figs. 5(a)–5(d) when $VO_2$ is at a low temperature. In the transmission state, the four-layer structure areas all participate in resonance on the account that all of them contain the strongest part of the electric field concentration at the resonance frequency. As manifested in the characteristics of the EM distribution map, it can be regarded that there are two opposing electrodes. The part with a strong electric field can be seen as the positive electrode, and the part with a weak electric field can be considered as the negative electrode. So, it is feasible to deduce the direction of the electric field from the figure, as noted by the black arrow. The directions of the electric fields on the $x$ axis are opposite in Figs. 5(a) and 5(b), which means a circulation can be approximately formed between the two layers. Therefore, induced magnetic fields are generated, and the magnetic dipoles

**Table 2. Function Menu of the Designed MS**

| The Direction of the Incident EM Waves | Function | Propagation State | Type of PC | $VO_2$ Is Excited | Operating Bandwidth | Relative Band (RB) |
|---|---|---|---|---|---|---|
| Forward | ① | Transmission | LTC | × | 0.57–0.83 THz | 37.3% |
| Forward | ② | Reflection | LTC | √ | 0.83–1.20 THz | 36.4% |
| | ④ | Reflection | LTL | √ | 1.19–1.41 THz | 16.9% |
| Backward | ③ | Reflection | LTC | √ | 0.83–1.17 THz | 34.0% |
| | ④ | Reflection | LTL | √ | 1.16–1.37 THz | 16.6% |

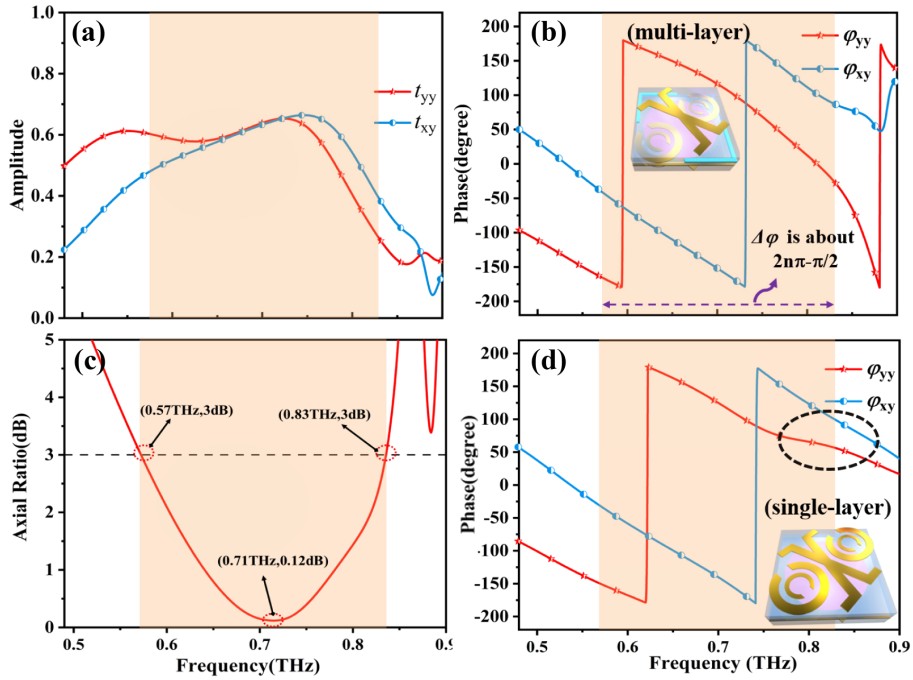


**Fig. 4.** Diagrams of (a) the amplitude, (b) the phase, and (c) the AR curves in function; (d) phase of the previous structure.

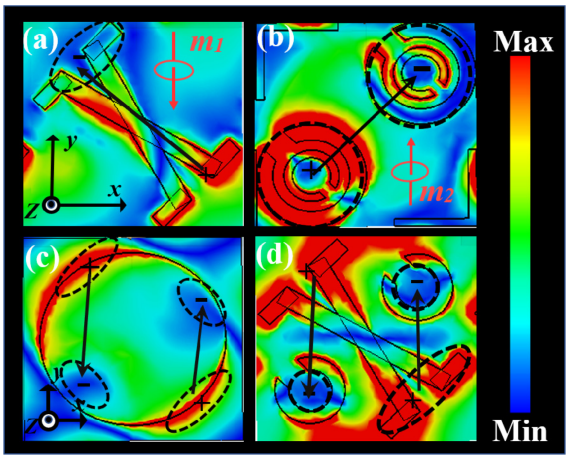


**Fig. 5.** Instantaneous electric field distributions in (a) the upper layer, (b) the second layer, (c) the middle layer, and (d) the bottom of the metal resonator at 0.71 THz in the transmission state.

are denoted by $m_1$ and $m_2$. Both induced magnetic fields can be decomposed into an $x$ axis component and a $y$ axis component. Between them, the $x$ component is vertical to $\boldsymbol{E}$, the incident electric field, so no PC occurs. However, the $y$ axis component is parallel to $\boldsymbol{E}$, thus creating the PC. Similarly, the electric field distributions of the remaining two layers are exhibited in Figs. 5(c) and 5(d). The electric field and the distribution of the two groups of electrodes are nearly the same, which can be seen approximately as forming electric resonators. Similarly, after decomposing the induced electric field into an $x$ axis component and a $y$ axis component along the coordinate axes, the part of the $x$ axis component is perpendicular to $\boldsymbol{E}$, contributing to the PC. And the part of the $y$ axis component is parallel to $\boldsymbol{E}$, achieving no PC.

Actually, not all EM waves will be vertically irradiated on the polarization converter in practical engineering, so maintaining performance stability under different conditions of the angle incidence is also essential. Figure 6 displays the variation in the AR change with the increase of the incident angle (IA). The bandwidth of AR < 3 dB remains slight change while increasing the incidence angle to 30°. When the IAs are greater than 30°, the deterioration of 3 dB frequency band does not appear. Instead, there is a band extension from 0.47 THz to 0.89 THz due to a significant expansion in the low-frequency region, and the RB increased from 37.1% to 61.8%. Therefore, it maintains outstanding CP characteristics, indicating the robustness of large-angle incidence. Benefiting from this property, the mentioned MS possesses bright potential application value in many practical occasions, such as wavefront detection, biomedical imaging, and atmospheric environment detection.

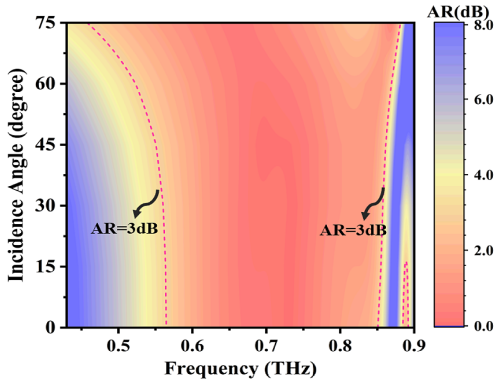


**Fig. 6.** Diagram of AR with IA increased in the function.

### B. Functions (② and ④) for the Forward Propagation in the Reflection State

Nevertheless, the $VO_2$ sheet switches into the metallic phase when the temperature exceeds 68°C. With a conductivity of up to $3 \times 10^5\ S\,m^{-1}$, $VO_2$ behaves as a reflective metal substrate that is capable of manipulating both forward and backward propagating EM waves in the design. In other words, this change successfully realizes the switch of transmission and reflection functions. In this section, the reflection of the forward propagation wave is mainly discussed.

For forward propagation, two functions of PC can be achieved in different bands. Herein, Figs. 7(a)–7(c) vividly demonstrate the amplitude, phase, and AR of the forward reflection waves when LTC PC occurs. As highlighted in the orange area, the value of $r_{xy}$ is close to the $r_{yy}$. In the meantime, it is sensible to take the transmission response into account for a more comprehensive judgment. The transmission coefficients $t_{yy}$ and $t_{xy}$ are both less than 0.1 in the operating band, which indicates that the transmission response is so weak that it can be ignored to a certain extent. As to the phase difference, the $\varphi_{yy}$ and $\varphi_{xy}$ keep the same rate of descent, maintaining a 90° phase difference continuously in Fig. 7(b). By combining the conditions of amplitude and phase, the MS achieves the AR < 3 dB band from 0.83 THz to 1.20 THz. The first frequency point is at 0.89 THz and remains below 0.1 until 1.12 THz, which satisfies good CP wave characteristics. By virtue of 36.4% RB, the MS meets the ultra-broadband indicator. The phase condition of the structure whose resonators are all on the top substrate layer is relatively messy as revealed in Fig. 7(d), which is conspicuous compared with Fig. 7(b). As mentioned above, the air layer supported by the L-shaped structure plays a crucial role in improving the phase by introducing optical path differences. Meanwhile, the change of the optical path difference implies the phase difference. As a result, the L-shaped backing plates are placed diagonally across the structure, effectively ameliorating the phase of $r_{xy}$, while having little effect on the phase of $r_{yy}$.

Moreover, the broadband of LTL PC can be achieved in the range of 1.19–1.41 THz. When there are EM incidents, the reflection amplitude curves are represented by the red and blue curves while the pink and purple curves describe the reflection phase in Fig. 7(e) and the curve of PCR is exhibited in Fig. 7(f). The amplitude of the cross-polarization reflection $r_{xy}$ is over 0.8, and the co-polarization reflection $r_{yy}$ is adjacent to 0.15, with $\Delta\varphi$ of $\phi$, which means the phase difference is basically satisfied. In 1.24–1.36 THz, the PCR curve draws near to 1, thus getting the broadband of LTL PC.

To get a deeper comprehension of the PC mechanism, the surface currents of function ②, which works in the forward reflection, provide a valuable illustration at 0.89 THz in Fig. 8. The current components along the axes are indicated by red arrows, and the overall surface current flow is represented by black arrows. Meanwhile, the current that has little effect on resonance is omitted for clearer analysis. As displayed in Fig. 8(a), the generating surface current $I_1$ flows down at a 45° angle along the edge of the top resonator. In Fig. 8(b), $I_2$ flows down along the edge of the C-shaped split resonator, which is also down 45° as well. As to the $VO_2$-integrated gold sheet in Fig. 8(c), the surface current $I_3$ is inclined 45° upward along the material boundary, whose direction is roughly opposite to the current $I_1$ and $I_2$. Thus, these opposite currents are expected to generate magnetic moments and induce a magnetic field $\boldsymbol{H}$ according to the right-hand rule. The magnetic field is decomposed into components along the $y$ axis and along the $x$ axis, denoted by $\boldsymbol{H_y}$ and $\boldsymbol{H_x}$. The $\boldsymbol{H_x}$ in the $x$ direction is perpendicular to $\boldsymbol{E}$ without polarization. The $\boldsymbol{H_y}$ in the $y$ direction is parallel to $\boldsymbol{E}$, which will generate an electric field in the $x$ direction, thus contributing to LTC PC.

Similarly, surface currents at 1.31 THz, which are displayed in Fig. 9, provide a valuable illustration of the principle for the forward LTL PC. In like manner, the current components along the axes are indicated by black arrows, and the overall surface current flow is represented by red arrows. As is explicitly demonstrated in Fig. 9(a), the surface current changes dramatically in this case compared to Fig. 8(a) whose current flows from top

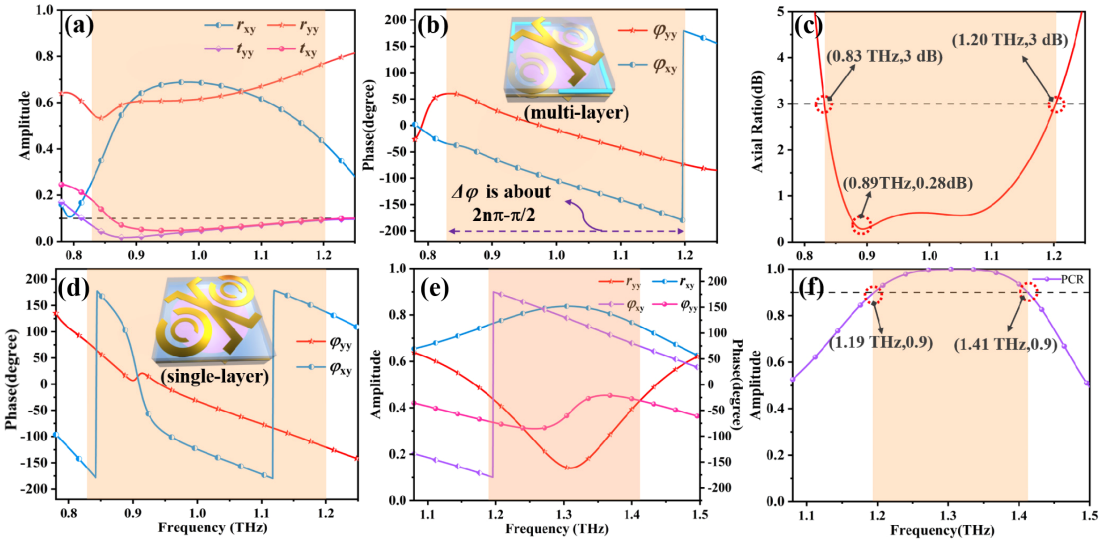


**Fig. 7.** Diagrams of (a) the amplitude, (b) the phase, (c) and the AR and (d) the phase of previous structure for the function ②. The diagrams of (e) the amplitude and phase, and (f) the PCR for the function ④.

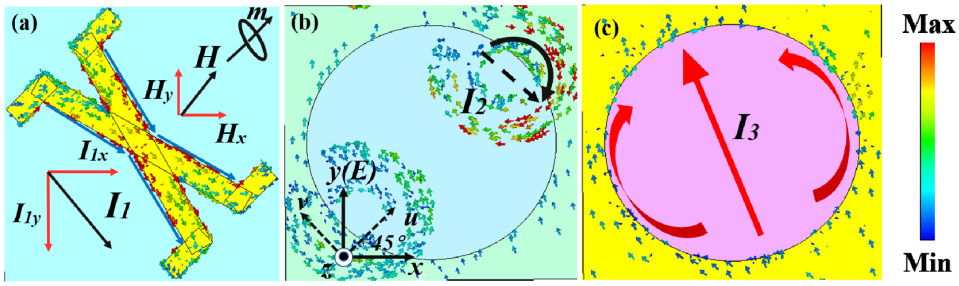


**Fig. 8.** Surface current diagrams of function ②: (a) on the top layer, (b) on the middle layer, and (c) on the bottom layer at 0.89 THz.

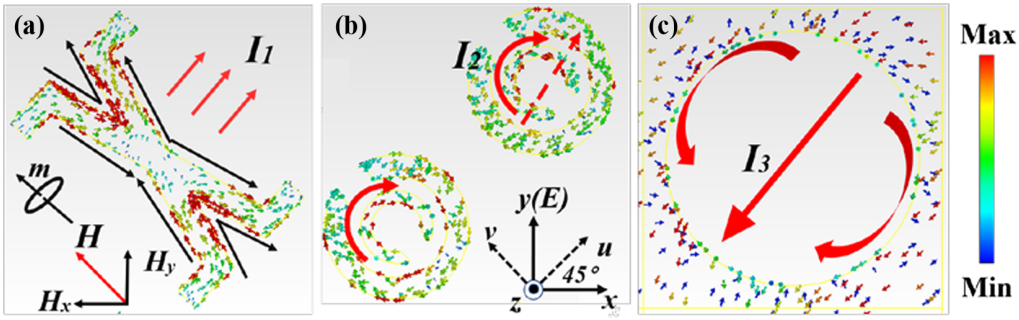


**Fig. 9.** Surface current diagrams of function ④: (a) on the top layer, (b) on the middle layer, and (c) on the bottom layer at 1.31 THz.

to bottom. The current generating surface current $I_1$ flows up at a 45° angle, as well as the direction of $I_2$ on the middle layer. Nevertheless, the direction of $I_3$ on the $VO_2$-integrated gold sheet is opposite to $I_1$ and $I_2$, which is likely to form a circulation and generate magnetic moments, thus inducing a magnetic field $H$. Then H can be decomposed into components along the $y$ axis and $x$ axis, denoted by $\boldsymbol{H_y}$ and $\boldsymbol{H_x}$. Considering that $\boldsymbol{H_x}$ in the $x$ direction has the opposite direction to $\boldsymbol{E}$, the original $y$-polarized LP wave is weakened. Meanwhile, a new electric field will generate in the $x$ direction on the ground that the $\boldsymbol{H_y}$ in the $y$ direction is parallel to $\boldsymbol{E}$, thus contributing to LTL PC.

### C. Functions (③ and ④) for the Backward Propagation in the Reflection State

The fruitful progress and breakthrough toward the wave of manipulation in transmissive or reflective converters have facilitated strong aspirations toward full-space wave control, not just in half-space. Herein, for a backward incidence, the backside of the MS can be utilized to obtain functions ③ and ④.

Similar to the forward reflection, LTC PC and LTL PC can be implemented as well for the backward incident waves. The curves of the amplitude, phase difference, and AR are revealed in Figs. 10(a)–10(c). In the range of 0.83–1.17 THz, the phase difference of $r_{yy}$ and $r_{xy}$ curves, whose values are approaching each other, is satisfied with a 90° phase difference synchronously. In like manner, the transmission response is weak on the ground, and the corresponding transmission coefficients both stay below 0.1 in the operating band. In addition, the operating band of the AR < 3 dB ranges from 0.83 THz to 1.17 THz with a RB of 33.54%, and the AR at the resonant point is almost equal to zero, which has excellent CP characteristics. Function ④ of a broadband LTL PC can be obtained too in 1.16–1.37 THz. The information about the PCR is manifested in Fig. 10(d).

Moreover, on account that the dependence on the IA is a key factor to assess the performance of a converter, the analysis of the IA influence on the AR is within the scope of our discussion. Based on the IA of two reflection functions ② and ③ noted above being relatively similar, their analyses of IA are displayed in Figs. 11(a) and 11(b). Their 3 dB bandwidth of AR remains basically invariant when the angle rises from 0° to 45°, possessing favorable stability of a large IA. However, as the IA continues to increase, a severe deterioration will occur in the higher operating frequency band in both Figs. 11(a) and 11(b), contributing to a significant reduction in the band of AR < 3 dB. Moreover, when the angle increases to 60°, there is a significant deterioration in the center of the working band in Fig. 11(a). Their frequency bandwidth meets the requirement only in the range of 0.83–0.94 THz finally. Chances are that, when the IA is greater than 45°, the original conditions such as phase and amplitude are difficult to meet, leading to this upset situation to appear. In view of the angular stability up to 45°, the IA of function ② and function ③ basically meets the standard of large-angle incidence stability to a certain degree.

## 4. PARAMETER DISCUSSION

Through utilizing simulation software, the geometrical parameters of the MS are optimized to obtain the widest bandwidth and the best performance of the AR as much as possible. It needs to be emphasized that the thicknesses of dielectric substrates are important variables on account that the AR is sensible to their change of value.

Figures 12(a) and 12(b) depict the impact of parameter $h_3$ on the AR under transmission and reflection conditions, respectively. With $h_3$ changing from 11 μm to 17 μm, the effect on the bandwidth of AR < 3 dB is not very significant, which remains unchanged in the transmission state. However, in terms of CP

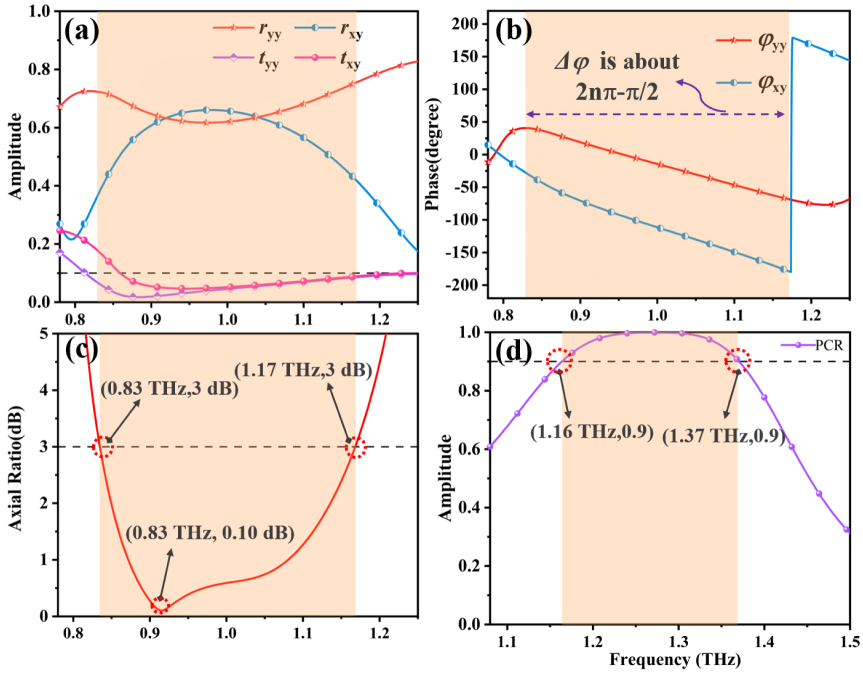


**Fig. 10.** Curves plots of (a) the amplitude, (b) the phase, (c) and the AR for the function ③. The curves plots of (d) the amplitude and phase, and (e) the PCR for the function ④.

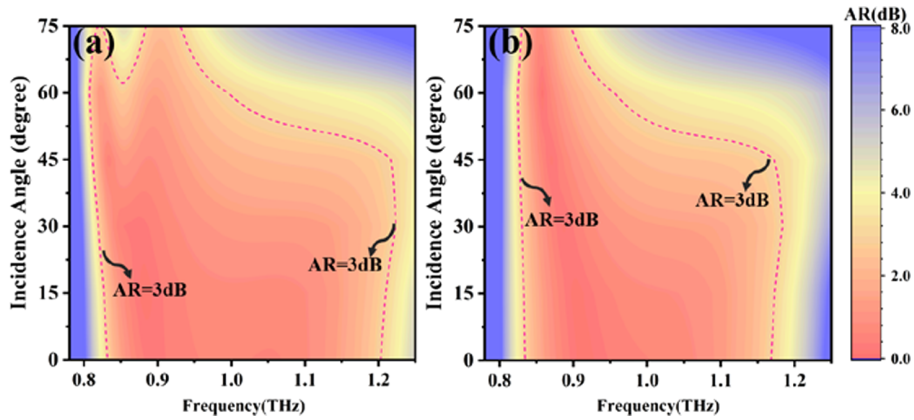


**Fig. 11.** Diagrams of AR with the incidence angle increased in the functions ② and ③, respectively.

characteristics, it is undeniable that $h_3 = 11$ μm and 13 μm are better options compared to other values. In the forward propagation reflection state, the band of AR < 3 dB decreases sharply at high frequency as the value of $h_3$ increases. The reason is that, as the thickness of the upper layers of the MS increases, it becomes more difficult for the forward transmitted and then reflected waves to match the amplitude and phase conditions. It is apparent that the AR remains around 0.5 in the range of 0.88 to 1.12 THz with $h_3 = 13$ μm while the AR of $h_3 = 11$ μm is greater than 1 in this band. Thereby, the CP characteristics are significantly enhanced compared to $h_3 = 11$ μm although the bandwidth is slightly reduced when $h_3 = 13$ μm. In other words, it is advisable to sacrifice a little operating bandwidth for an obvious upgrade in CP characteristics. As a result, it is more appropriate to select $h_3 = 13$ μm. In like manner, the changing trend of the AR varied with the dielectric thickness $h_4$ from 15 to 21 μm, and the identical span of 1.5 μm is presented in Fig. 12(c). For a comprehensive consideration to acquire the best performance under the backward reflection state, $h_4 = 18$ μm is a sensible option in that it holds the advantages of wide bandwidth and superior CP characteristics simultaneously in this case. Furthermore, the parameter $w_1$ also has a certain implication on AR under the three functions as displayed in Figs. 12(d)–12(f). In general, the operating band of the device is blueshifted as $w_1$ increases, and perfect CP waves can be achieved at the frequency point. Through comprehensive consideration of the working bandwidth, CP characteristics, and stable performance, $w_1 = 7$ μm is the best choice. Other parameters cannot contribute to an obvious impact, and the MS is relatively insensitive to them.

Finally, to exhibit definite innovation concerning the proposed MS based on $VO_2$, Table 3 is given to make a comparison between $VO_2$ and other phase change materials, which helps us better comprehend the situation of related work. Phase change

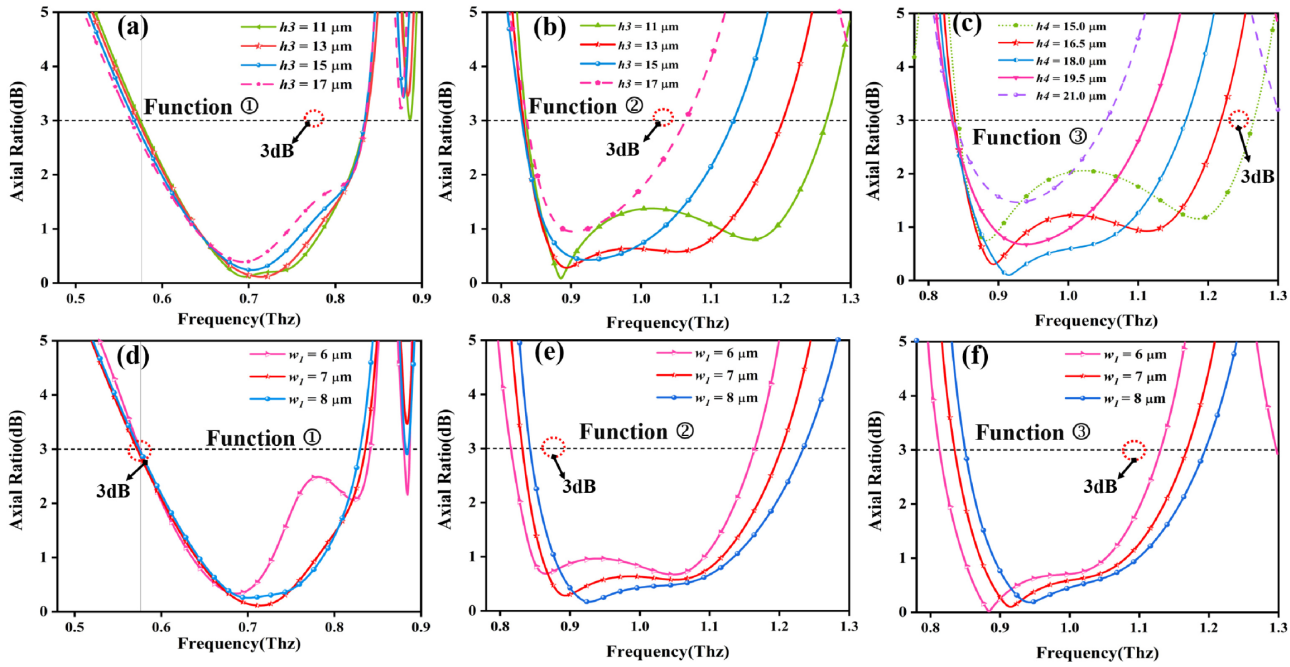


**Fig. 12.** Parameters discussion about the effects of the height of the dielectric substrate $h_3$, $h_4$, and $w_1$ on the AR under different functions.

**Table 3. Comparisons between This Work and Reported Switchable and Multitasking Devices**

| | | | | Functions and Operating Bands | | |
|---|---|---|---|---|---|---|
| **Refs.** | **Phase Change Material** | **External Variables** | **Adjustment Object** | **Absorber** | **LTL PC** | **LTC PC** |
| [41] | Graphene (THZ) | Voltage | LTL or LTC PC | × | 36.9–38.8 | 35.8–39.9 |
| [42] | | | LTL or LTC PC | × | 0.40–0.95 | 0.47–0.67 |
| [43] | Liquid crystal(GHz) | Voltage | Working point | 11.04 → 10.21 | × | × |
| [44] | | | Working point | 381.8 → 421.2 | × | × |
| [45] | ITO (GHz) | —— | Achieve absorb | ✓ | 20.8–54.1 | × |
| [36] | $VO_2$ (THz) | Thermal | LTL or LTC PC | × | 0.91–2.15 | 1.07–1.67 |
| This work | | | Transmission → Reflection | × | Broadband | Ultra-broadband |

material, external variables, adjustment objects, functions, and operating bands in different works are all listed. It can be seen that the devices proposed in many papers have excellent performance, though the devices proposed in this paper also have irreplaceable characteristics in that they can switch between transmission state and reflection state, and there are four different functions of PC, which are not only limited to forward propagation wave and have broad prospects for full-space manipulation of EM waves.

## 5. CONCLUSION

In conclusion, a multifunctional MS that enables the ultra-broadband LTC PC based on $VO_2$ both in transmission and reflection states is proposed. Comprehensive simulation results demonstrate that the MS can implement AR < 3 dB band from 0.57 THz to 0.83 THz with a RB of 37.3%. The MS is switched from the transmission to reflection state when the temperature exceeds 68°C. In the reflection state, the operating band of AR < 3 dB in the range of 0.83–1.20 THz and 0.83–1.17 THz can be, respectively, obtained with RBs of 36.4% and 34.0%, respectively, for the forward propagation and the backward one. Meanwhile, the function of a broadband LTL PC can be achieved. In addition, the polarization mechanisms are illustrated based on electric field distribution and surface current diagrams. And the influences of IA and the discussion of structural parameters are manifested as well. Thus, the proposed structure holds promising applications in EM wave steering, THz modulation, stealth technology, communication systems, and so on.

**Disclosures.** The authors declare no conflicts of interest.

**Data availability.** Data underlying the results presented in this paper are not publicly available at this time but may be obtained from the authors upon reasonable request.

## REFERENCES

1. J. Hao, Y. Yuan, L. Ran, T. Jiang, J. A. Kong, C. T. Chan, and L. Zhou, "Manipulating electromagnetic wave polarizations by anisotropic metamaterials," Phys. Rev. Lett. **99**, 063908 (2007).
2. D. R. Smith, J. B. Pendry, and M. C. K. Wiltshire, "Metamaterials and negative refractive index," Science **305**, 788–792 (2004).
3. J. B. Pendry, A. J. Holden, and W. J. Stewart, "Extremely low frequency plasmons in metallic mesostructures," Phys. Rev. Lett. **76**, 4773–4776 (1996).

4. J. Yang, S. Chen, M. Chen, J. C. Ke, M. Z. Chen, C. Zhang, R. Yang, X. Li, Q. Cheng, and T. J. Cui, "Folded transmitarray antenna with circular polarization based on metasurface," IEEE Trans. Antennas Propag. **69**, 806–814 (2020).
5. D. Liu, H. T. Yu, Z. Yang, and Y. Y. Duan, "Ultrathin planar broadband absorber through effective medium design," Nano Res. **9**, 2354–2363 (2016).
6. J. Hao, Y. Yuan, L. Ran, T. Jiang, J. A. Kong, C. T. Chan, and L. Zhou, "Broadband polarizers based on graphene metasurfaces," Opt. Lett. **41**, 5592–5595 (2016).
7. Y. Su, H. Zhou, Y. M. Wang, and H. P. Shen, "A novel polarization demodulation method using polarization beam splitter (PBS) for dynamic pressure sensor," Opt. Fiber Technol. **41**, 69–73 (2018).
8. X. Jing, X. C. Gui, P. W. Zhou, and Z. Hong, "Physical explanation of Fabry–Pérot cavity for broadband bilayer metamaterials polarization converter," J. Lightwave Technol. **36**, 2322–2327 (2018).
9. J. X. Zhao, B. X. Xiao, X. J. Huang, and Y. H. Lin, "Multiple-band reflective polarization converter based on complementary L-shaped metamaterial," Microw. Opt. Technol. Lett. **57**, 978–983 (2015).
10. L. Zhang, P. Zhou, H. Lu, L. Zhang, J. Xie, and L. Deng, "Realization of broadband reflective polarization converter using asymmetric cross-shaped resonator," Opt. Mater. Express **6**, 1393–1404 (2016).
11. N. Yu and F. Capasso, "Flat optics with designer metasurfaces," Nat. Mater. **13**, 139–150 (2014).
12. R. D. King-Smith and D. Vanderbilt, "Theory of polarization of crystalline solids," Phys. Rev. B **47**, 1651–1654 (1993).
13. J. A. Davis, I. Moreno, and P. Tsai, "Polarization eigenstates for twisted-nematic liquid-crystal displays," Appl. Opt. **37**, 937–945 (2018).
14. J. Shabanpour, S. Beyraghi, and H. Oraizi, "Reconfigurable honeycomb metamaterial absorber having incident angular stability," Sci. Rep. **10**, 14920 (2020).
15. J. Shabanpour, S. Beyraghi, F. Ghorbani, and H. Oraizi, "Implementation of conformal digital metasurfaces for THz polarimetric sensing," OSA Contin. **4**, 1372–1380 (2021).
16. Y. Lee, S. J. Kim, and J. G. Yun, "Electrically tunable multifunctional metasurface for integrating phase and amplitude modulation based on hyperbolic metamaterial substrate," IEEE Trans. Microw. Theory Tech. **26**, 32063–32073 (2018).
17. H.-P. Li, G.-M. Wang, T. Cai, J.-G. Liang, and X.-J. Gao, "Phase- and amplitude-control metasurfaces for antenna main-lobe and side-lobe manipulations," IEEE. Trans. Antennas Propag. **66**, 5121–5129 (2018).
18. X. Gao, X. Han, W. P. Cao, H. O. Li, H. F. Ma, and T. J. Cui, "Ultrawideband and high-efficiency linear polarization converter based on double V-shaped metasurface," IEEE Trans. Antennas Propag. **63**, 3522–3530 (2015).
19. M. A. Choubar, M. Farahani, A. R. Sebak, and T. A. Denidni, "Ka-band linear to circular polarization converter based on multilayer slab with broadband performance," IEEE Access **5**, 17927–17937 (2017).
20. N. K. Grady, J. E. Heyes, D. R. Chowdhury, Y. Zeng, and A. K. Azad, "Terahertz metamaterials for linear polarization conversion and anomalous refraction," Science **340**, 1304–1307 (2013).
21. T. Q. H. Nguyen, T. K. T. Nguyen, and T. Q. M. Nguyen, "Simple design of a wideband and wide-angle reflective linear polarization converter based on crescent-shaped metamaterial for Ku-band applications," Opt. Commun. **486**, 126773 (2021).
22. H. B. Wang, Y. J. Cheng, and Z. N. Chen, "Dual-band miniaturized linear-to-circular metasurface polarization converter with wide-band and wide-angle axial ratio," IEEE Trans. Antennas Propag. **69**, 9021–9025 (2021).
23. X. M. Liu, Y. X. Zhou, C. Wang, L. Gan, X. F. Yang, and L. J. Sun, "Dual-band dual-rotational-direction angular stable linear-to-circular polarization converter," IEEE Trans. Antennas Propag. **70**, 6054–6059 (2022).
24. C. Huang, C. Zhang, J. Yang, B. Sun, B. Zhao, and X. Luo, "Reconfigurable metasurface for multifunctional control of electromagnetic waves," Adv. Opt. Mater. **5**, 1700485 (2017).
25. Q. Y. Wen, H. W. Zhang, Q. H. Yang, Z. Chen, Y. Long, Y. L. Jing, Y. Lin, and P. X. Zhang, "A tunable hybrid metamaterial absorber based on vanadium oxide films," J. Phys. D **45**, 235106 (2012).
26. J. M. Wu and L. B. Liou, "Room temperature photo-induced phase transitions of $VO_2$ nanodevices," J. Mater. Chem. **21**, 5499–5504 (2011).
27. H. L. Zhu, Y. Zhang, L. F. Ye, Y. K. Li, Y. H. Xu, and R. M. Xu, "Switchable and tunable terahertz metamaterial absorber with broadband and multi-band absorption," Opt. Express **28**, 38626–38637 (2020).
28. M. Heidari, V. Faramarzi, Z. Sharifi, and M. Hashemi, "A high-performance TE modulator/TM-pass polarizer using selective mode shaping in a $VO_2$-based side-polished fiber," Nanophotonics **10**, 3451–3463 (2021).
29. A. Zimmers, L. Aigouy, M. Mortierer, and A. Sharoni, "Role of thermal heating on the voltage induced insulator-metal transition in $VO_2$," Phys. Rev. Lett. **110**, 056601 (2013).
30. Y. Ren and B. Tang, "Switchable multi-functional $VO_2$-integrated metamaterial devices in the terahertz region," J. Lightwave Technol. **39**, 5864–5868 (2021).
31. M. Heidari and S. Bahadori-Haghighi, "Design and analysis of a polarization-insensitive $VO_2$/graphene optical modulator using a 3D heat transfer method," ACS Appl. Electron. Mater. **4**, 4042–4050 (2022).
32. L. Lei, F. Lou, K. Y. Tao, H. X. Huang, X. Cheng, and P. Xu, "Tunable and scalable broadband metamaterial absorber involving $VO_2$-based phase transition," Photon. Res. **7**, 734–741 (2019).
33. S. Yuan, R. C. Yang, J. P. Xu, J. Y. Wang, and J. P. Tian, "Photoexcited switchable single-/dual-band terahertz metamaterial absorber," Mater. Res. Express **6**, 075807 (2019).
34. L. Long, S. Taylor, and L. Wang, "Enhanced infrared emission by thermally switching the excitation of magnetic polariton with scalable microstructured $VO_2$ metasurfaces," ACS Photon. **7**, 2219–2227 (2020).
35. R. Yahiaoui, Z. A. Chase, C. Kyaw, E. Seabron, J. Mathews, and T. A. Searles, "Dynamically tunable single-layer $VO_2$/metasurface based THz cross-polarization converter," J. Phys. D **54**, 235101 (2021).
36. D. X. Yan, Q. Y. Feng, Z. W. Yuan, M. Meng, X. J. Li, G. H. Qiu, and J. N. Li, "Wideband switchable dual-functional terahertz polarization converter based on vanadium dioxide-assisted metasurface," Chin. Phys. B **31**, 014211 (2022).
37. J. Shabanpour, "Programmable anisotropic digital metasurface for independent manipulation of dual-polarized THz waves based on a voltage-controlled phase transition of $VO_2$ microwires," J. Mater. Chem. C **8**, 7189–7199 (2020).
38. J. P. Fan and Y. Z. Cheng, "Broadband high-efficiency cross-polarization conversion and multi-functional wavefront manipulation based on chiral structure metasurface for terahertz wave," J. Phys. D **53**, 025109 (2019).
39. C. F. Chen, C. T. Ku, Y. H. Tai, P. K. Wei, H. N. Lin, and C. B. Huang, "Creating optical near-field orbital angular momentum in a gold metasurface," Nano Lett. **15**, 2746–2750 (2015).
40. Y. Z. Sun, C. J. Gao, J. Qu, and H. F. Zhang, "Circularly polarized manipulations with $VO_2$-doped dielectric electromagnetically induced transparency and absorption," Ann. Phys. (Berlin) **534**, 2200130 (2022).
41. H. J. Zhang, Y. Liu, Z. Q. Liu, X. S. Liu, G. Q. Liu, and G. L. Fu, "Multi-functional polarization conversion manipulation via graphene-based metasurface reflectors," Opt. Express **29**, 70–81 (2021).
42. X. Y. Yu, X. Gao, W. Qiao, L. L. Wen, and W. L. Yang, "Broadband tunable polarization converter realized by graphene-based metamaterial," IEEE Photon. Technol. Lett. **28**, 2399–2402 (2016).
43. J. F. Lv, C. Ding, F. Y. Meng, J. Q. Han, T. Jin, and Q. Wu, "A tunable metamaterial absorber based on liquid crystal with the compact unit cell and the wideband absorption," Liq. Cryst. **48**, 1438–1447 (2021).
44. J. Yang, P. Wang, T. Shi, S. Gao, and H. B. Lu, "Electrically tunable liquid crystal terahertz device based on double-layer plasmonic metamaterial," Opt. Express **27**, 27039–27045 (2019).
45. L. Dong, B. Z. Zhang, J. P. Duan, Y. H. Yang, and Y. P. Liu, "Conformal transparent metamaterials inducing ultra-broadband absorption and polarization conversion," J. Infrared Millimeter Terahertz Waves **40**, 905–916 (2019).